

Bounds on Λ at the Galactic Center

Prajwal Hassan Puttasiddappa^{1,2,3}, Muzammil Mushtaq⁴, Willian Ramirez^{2,5}, David F. Mota¹

¹Institute of Theoretical Astrophysics, University of Oslo, Norway

²PPGCosmo, Universidade Federal do Espírito Santo, Brazil

³Departamento de Física Teórica, Universidade do Estado do Rio de Janeiro, Brazil

⁴Zentrum für Astronomie, Heidelberg University, Germany

⁵Centro Brasileiro de Pesquisas Físicas, Brazil

Corresponding author: prajwal.puttasiddappa@edu.ufes.br

June 12, 2026

Abstract

We constrain the cosmological constant Λ using astrometric and spectroscopic observations of the S2, S1, and S14 stars orbiting Sgr A*. The stellar motion is modelled by numerically integrating timelike geodesics in Schwarzschild-de Sitter spacetime, including relativistic redshift and time-delay corrections. Orbital and spacetime parameters are inferred using a Bayesian MCMC analysis. The resulting posterior distributions place upper bounds on the magnitude of Λ at the Galactic Center (GC). Combining the independent constraints from the S2, S1, and S14 orbits yields upper bounds of $\Lambda \lesssim 6.9 \times 10^{-48} \text{m}^{-2}$ at 68% credibility and $\Lambda \lesssim 1.0 \times 10^{-38} \text{m}^{-2}$ at 95% credibility.

1 Introduction

Standard cosmological probes, including Type Ia supernovae [1, 2], Baryon Acoustic Oscillations [3, 4, 5], and the Cosmic Microwave Background (CMB) [6], have firmly established the existence of Dark Energy as the driver of the Universe’s late-time accelerated expansion. While recent results from the Dark Energy Spectroscopic Instrument (DESI) have hinted at a possible time evolution in the dark-energy equation of state [7, 8, 9], the evidence remains inconclusive. In particular, the statistical significance depends sensitively on the choice of complementary supernova datasets and the adopted dark-energy parameterization, and currently remains below the 5σ discovery threshold [10]. Within the standard cosmological model, known as Λ CDM, the cosmological constant, Λ , provides the minimal and most successful phenomenological description of the observed accelerated phase. Although its dynamical influence becomes appreciable on cosmological scales, its manifestation in local, gravitationally bound systems remains a subject of interest.

The influence of dark energy on the dynamics of the Local Group and proximal galaxy clusters has been extensively studied in the literature [11, 12, 13, 14, 15, 16, 17, 18] (also see, [19]). In such systems, the repulsive linear force associated with Λ competes with Newtonian attraction. This competition defines the zero-velocity radius, the critical scale at which cosmological repulsion exactly counteracts the inward gravitational acceleration. This force balance plays a central role in explaining the observed ‘*quietness*’ of the local Hubble flow, wherein the presence of Λ suppresses peculiar velocity dispersion and promotes a nearly linear expansion in the periphery of bound systems. Moreover, the inclusion of Λ necessitates a re-evaluation of the timing argument [20] employed to infer the total mass of systems such as the Milky Way-Andromeda pair [21, 22, 23, 24, 25, 26, 27].

In this work, we exploit observables from the Galactic Center (GC) to derive an upper bound on Λ . As summarized in Table 1, existing constraints on Λ span a vast range of physical scales, from planetary motions in the Solar System to gigaparsec-scale observations of the CMB. The inferred upper limits exhibit a scale dependence, with local gravitational systems typically admitting weaker constraints than those derived from cosmological observations. Within this hierarchy, the GC occupies an intermediate regime, thereby providing a complementary avenue for constraining the imprint of Λ in a comparatively strong gravitational environment. The GC has emerged as one of the most incisive laboratories for probing gravity in the high-mass, strong-field regime. At its core resides Sagittarius A* (Sgr A*), a supermassive compact object whose immediate environment provides two principal observational channels for testing gravity: the imaging of its shadow and the monitoring of stellar orbits. Together, these observables facilitate a systematic comparison between General Relativity (GR) and its theoretical extensions.

Recent advances in very-long-baseline interferometry have opened a new observational window into the immediate vicinity of the central compact object at the GC. In particular, the Event Horizon Telescope (EHT) has resolved horizon-scale features of the candidate supermassive black holes (SMBHs) in Messier 87* [28] and Sgr A* [29]. While these observations provide strong electromagnetic evidence for compact objects broadly consistent with the Kerr geometry, current uncertainties in shadow-size measurements still permit departures from GR. Consequently, the angular diameter of the black hole (BH) shadow, particularly in the case of Sgr A*, which probes higher curvature scales than M87*, remains a vital diagnostic for placing constraints on the underlying spacetime structure [30].

The dynamics of stars kinematically bound to the central mass offer a supplementary probe of the gravitational field at scales that have previously lacked such precise empirical access. Decades of monitoring by facilities such as the Keck Observatory [31, 32] and the Very Large Telescope (VLT) [33] with a more recent enhancement by the sub-milliarcsecond astrometry of the GRAVITY instrument [34] have tracked a cluster of young, massive stars called ‘S-stars’, with unprecedented accuracy [35, 36]. Within this cluster, the S2 (or S0-2) star occupies a distinguished role due to its short orbital period (~ 16 years), high eccentricity, and well-resolved pericentre passage. Its trajectory penetrates deep into the gravitational potential of Sgr A*, reaching velocities of nearly 3% of the speed of light. The motion provides access to leading-order post-Newtonian effects, including the gravitational redshift [37, 38] and Schwarzschild periapsis precession [39].

The precise tracking of S2’s trajectory has enabled stringent tests of a broad class of modified gravity scenarios, including Scalar–Tensor–Vector gravity [40, 41], $f(R)$ gravity [42], and the broader class of Horndeski models [43, 44]. Beyond modifications to the Einstein–Hilbert action, S2 observations serve to evaluate more exotic scenarios such as the presence of wormholes [45], naked singularities [46], or regular compact objects [47, 48]. Furthermore, the S2 orbit has been utilized to bound dark matter density profiles, including the potential for dense ‘spikes’ near the central mass and the presence of ultralight bosonic fields [49, 50, 51]. Also, the dynamics of S-stars and G-sources (a population of dust-enshrouded objects) have been employed to investigate dark matter-inspired alternatives to the central compact object paradigm, including dense self-gravitating fermionic configurations [52, 53, 54].

The two-body problem under the combined influence of dark energy and post-Newtonian corrections is studied in detail in [57], where the critical period $T_\Lambda = 2\pi/(c\sqrt{\Lambda})$ was introduced. Comparing this with the Keplerian orbital period $T_K = 2\pi\sqrt{a^3/GM}$ provides a heuristic criterion for assessing whether a binary system resides in a regime dominated by local gravitational dynamics ($T_K \ll T_\Lambda$) or one where cosmological effects become appreciable ($T_K \gg T_\Lambda$). More fundamentally, this hierarchy emerges naturally from the curvature structure of the Schwarzschild-de Sitter (SdS) spacetime. For example, using $a = r$ in T_K , the Kretschmann scalar ($K = R_{\alpha\beta\mu\nu}R^{\alpha\beta\mu\nu}$) may be expressed as,

Observed effect	Estimate on Λ (m^{-2})
<i>Solar System estimates</i>	
Light deflection	No constraint
Gravitational time delay [55]	$\lesssim 10^{-24}$
Geodetic precession [55]	$\lesssim 10^{-27}$
Gravitational redshift [55]	$\lesssim 10^{-28}$
Mercury Perihelion shift [55]	$\lesssim 10^{-41}$
Perihelion precessions of Earth and Mars [56]	$\lesssim 10^{-42}$
Perihelion precession of Saturn [57]	$\lesssim 10^{-46}$
<i>Astrophysical / Cosmological estimates</i>	
Binary pulsars [58]	$\lesssim 10^{-40}$
Lensing by Galaxy cluster [59]	$\lesssim 10^{-50}$
Galaxy rotation curves [60]	$\lesssim 1.9 \times 10^{-51}$
Local group [57]	$= (3.13 \pm 2.42) \times 10^{-52}$
Virgo cluster [57]	$> 1.58 \times 10^{-53}$
LSS/CMB [6]	$= (1.097 \pm 0.02) \times 10^{-52}$
SH0ES [61]	$= (1.29 \pm 0.05) \times 10^{-52}$
Supernovae Ia (Pantheon+) [62]	$\approx 1.1 \times 10^{-52}$

Table 1: Bound / inferred value of Λ from local, astrophysical, and cosmological scales.

$$K_{\text{SdS}} = K_{\text{Sch}} \left[1 + \frac{1}{72} \left(\frac{T_K}{T_\Lambda} \right)^4 \right], \quad (1)$$

where $K_{\text{Sch}} = 48G^2M^2/(c^4r^6)$ denotes the Schwarzschild contribution. This shows that the impact of Λ on a gravitationally bound system is governed by a ratio of timescales, rather than length scales. For the observed cosmological value of Λ , one finds $T_\Lambda \sim 60$ Gyr, whereas the orbital periods of the S-stars can range from a few decades to a few centuries, implying a large disparity between the two timescales, $T_K \ll T_\Lambda$. Despite probing a stronger gravitational potential than the Solar System, the characteristic curvature scales associated with S-star orbits remain broadly comparable to those encountered in outer Solar System planets. One may therefore anticipate constraints on Λ of a similar order of magnitude to existing Solar-System bounds.

In this work, we constrain Λ by modelling the relativistic orbits of the S2 star, supplemented by S1 and S14, and comparing them with publicly available astrometric and spectroscopic data. Moving beyond standard post-Newtonian approximations and isolated precession-based estimates, we perform a numerical integration of timelike geodesics in SdS spacetime. The parameters describing the spacetime geometry, stellar dynamics, and observational reference frame are jointly inferred for each star.

The remainder of this paper is organized as follows. In Section 2, we establish the basic formalism and available bounds on Λ from the shadow size of Sgr A* and the detected Schwarzschild precession of the S2 orbit. Section 3 details the relativistic orbit modelling, while Section 4 describes the used observational datasets and the MCMC implementation. Finally, in Section 5, we present the resulting constraints on Λ and discuss their implications, followed by concluding remarks in Section 6.

2 Constraints on Λ from S2 precession and black hole shadow

We model the stellar dynamics and light propagation in the Schwarzschild-de Sitter (SdS) spacetime, also known as the Kottler metric [63]. The line element in spherical coordinates

$\{t, r, \theta, \varphi\}$ is given by,

$$ds^2 = -f(r)dt^2 + \frac{1}{f(r)}dr^2 + r^2(d\theta^2 + \sin^2\theta d\varphi^2),$$

$$\text{where , } f(r) = \left(1 - \frac{2GM}{rc^2} - \frac{\Lambda r^2}{3}\right).$$
(2)

In the limit $\Lambda = 0$, the metric reduces to the Schwarzschild solution. For non-vanishing Λ , the spacetime is no longer asymptotically flat, and global quantities such as the Arnowitt–Deser–Misner (ADM) mass are not well-defined. Nevertheless, on the dynamical scales relevant to the S-stars and the photon trajectories, the parameter M remains an accurate characterization of the central gravitating mass.

Throughout this work, we assume a positive cosmological constant¹ ($\Lambda > 0$), consistent with the SdS structure. The horizons of the spacetime are determined by the roots of $f(r) = 0$. For $9\Lambda(GM/c^2)^2 < 1$, the metric admits two coordinate singularities corresponding to a BH horizon and the cosmological horizon. The orbits of interest lie in the static region between these two scales. The limiting case, $9\Lambda(GM/c^2)^2 = 1$ corresponds to the Nariai limit, where the two horizons coincide.

To describe both null and timelike motion, we consider geodesics satisfying the normalization condition $g_{\mu\nu}\dot{x}^\mu\dot{x}^\nu = -\epsilon c^2$, where $\epsilon = 0$ for null geodesics and $\epsilon = 1$ for timelike geodesics. Here, the overdot denotes differentiation with respect to an affine parameter λ , which, for the timelike case, is identified with the stellar proper time τ (i.e., $\dot{x}^\mu \equiv dx^\mu/d\tau$). Using the conserved specific energy $E = f(r)\dot{t}$ and the specific angular momentum $L = r^2\dot{\varphi}$ the radial equation of motion can be written as a one-dimensional system with an effective potential,

$$\dot{r}^2 = E^2 - V(r),$$

$$\text{with , } V(r) = \left(1 - \frac{2GM}{rc^2} - \frac{\Lambda r^2}{3}\right) \left(\epsilon c^2 + \frac{L^2}{r^2}\right).$$
(3)

Using the substitution $u = 1/r$, the equation (3) can be rewritten in terms of φ , (using $d/d\lambda = Lu^2 d/d\varphi$). Differentiating with respect to φ yields,

$$\frac{d^2u}{d\varphi^2} + u = \frac{3GM}{c^2}u^2 + \epsilon \left(\frac{GM}{L^2} - \frac{\Lambda c^2}{3L^2u^3}\right).$$
(4)

We exploit this framework to constrain Λ at the GC using the angular size of the Sgr A* shadow and the orbital precession of the S2 star. Both channels can quantify departures from the Schwarzschild geometry. Revisiting Λ bounds through these serves as a valuable diagnostic before executing a fit for the full stellar dynamics.

2.1 Black Hole Shadow

For null geodesics ($\epsilon = 0$), the equation (4) is independent of Λ [67], indicating that the effect of Λ on null trajectories arises not through the geodesic dynamics, but through the geometry of the spacetime. Also the equation (3) simplifies in terms of the impact parameter $b(r) = L/E$ to,

$$\frac{\dot{r}^2}{L^2} = \frac{1}{b^2} - \frac{f(r)}{r^2}.$$
(5)

A comprehensive review of the geometric definitions and conventions on black hole shadows is provided in [68]. From the turning point condition $\dot{r} = 0$, circular null orbits satisfy $b(r) =$

¹For a discussion on $\Lambda < 0$, see [64, 65, 66]

$r/\sqrt{f(r)}$. The radius and stability of these circular orbits are dictated by the first and second derivatives of the effective potential $V_\gamma(r) \equiv f(r)/r^2$, respectively. Specifically, the radius of the unstable photon sphere r_γ is determined by the extremum $\frac{d}{dr}[f(r)/r^2] = 0$. Evaluating this condition yields $r_\gamma = 3GM/c^2$, demonstrating that the radius of the photon sphere in SdS spacetime is independent of Λ [64].

The apparent boundary of the shadow is defined by null geodesics that asymptotically approach r_γ and is determined by the critical impact parameter $b_{\text{crit}} \equiv b(r_\gamma)$, which separates captured and escaping trajectories. It is given by,

$$b_{\text{crit}} = \frac{r_\gamma}{\sqrt{f(r_\gamma)}} = \frac{3\sqrt{3}(GM/c^2)}{\sqrt{1 - 9\Lambda(GM/c^2)^2}}. \quad (6)$$

In asymptotically flat spacetimes, b_{crit} directly defines the shadow radius for an observer at infinity. In contrast, because SdS spacetime is asymptotically de Sitter, ‘*impact parameter*’ becomes ill-defined. The observed angular size of the shadow depends explicitly on the observer’s position and motion [69, 70, 71]. For a static observer located at radial coordinate r_O between the BH event horizon and cosmological horizon, the angular size ϑ_{sh} is given by [71, 68],

$$\sin^2 \vartheta_{\text{sh}} = \frac{b_{\text{crit}}^2 f(r_O)}{r_O^2}. \quad (7)$$

A brief discussion of these geometric subtleties is provided in Appendix A. In the small-angle limit, the shadow radius is given by [30],

$$r_{\text{sh}} = \frac{3\sqrt{3}(GM/c^2)}{\sqrt{1 - 9\Lambda(GM/c^2)^2}} \sqrt{1 - \frac{2GM}{r_O c^2} - \frac{\Lambda r_O^2}{3}}. \quad (8)$$

This expression reduces to the standard Schwarzschild result $3\sqrt{3}GM/c^2$ provided the flat-space limit ($\Lambda \rightarrow 0$) is taken before the asymptotic observer limit ($r_O \rightarrow \infty$). A crucial distinction from the Schwarzschild case is the explicit dependence on the observer’s position r_O ; as the observer approaches the cosmological horizon, the metric function vanishes, causing the apparent angular size of the shadow to contract to a point [72].

For comparison with observational data, the shadow radius is typically expressed via the fractional deviation parameter δ , which quantifies the departure from the Schwarzschild prediction, $r_{\text{sh}} = 3\sqrt{3}GM(\delta + 1)/c^2$. Since the EHT measures the angular size of the shadow, any bound placed on the shadow radius r_{sh} is inherently dependent on the mass-to-distance ratio (M/D) of the BH. Consequently, the resulting constraints on δ (and by extension, Λ) are sensitive to the choice of M and D priors. To calibrate this scale, we utilize estimates derived from stellar orbits by the Keck [38] and GRAVITY [39] collaborations. The average of these dynamical estimates is typically used to translate angular observations into the r_{sh}/M constraints [29] shown in Figure 1 (in units of (c^2/G)). Current measurements imply $\Lambda \lesssim 10^{-41} \text{m}^{-2}$ [30] for an observer at $r_O \sim 8 \text{kpc}$.

2.2 S2 Orbital Precession

For timelike geodesics ($\epsilon = 1$), the second and third terms on the right-hand side of the equation (4) represent the Schwarzschild and the cosmological constant contributions, respectively. Treating these as perturbations around the Newtonian solution $u_N = \frac{GM}{L^2}(1 + e \cos \varphi)$, one obtains the periapsis advance per orbit [73, 74, 75, 76] (also derived in Appendix B)

$$\Delta\varphi \equiv \Delta\varphi_{\text{Schwarz}} + \Delta\varphi_\Lambda = \frac{6\pi GM}{c^2 a(1 - e^2)} + \frac{\Lambda \pi c^2 a^3}{GM} \sqrt{1 - e^2}. \quad (9)$$

The first term is the standard Schwarzschild precession, while a positive cosmological constant induces a small positive correction. To characterize deviations from the Schwarzschild

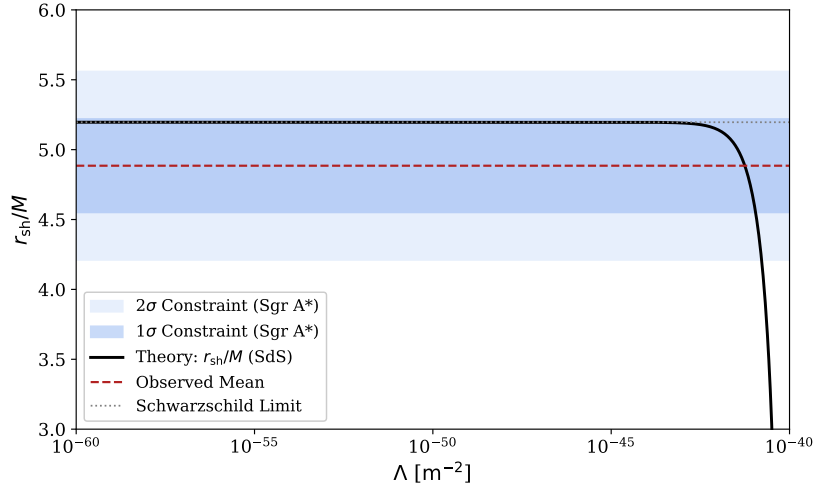


Figure 1: Shadow radius r_{sh}/M (in the units of c^2/G) as a function of the cosmological constant Λ for a static observer. The shaded bands represent the 1σ and 2σ observational constraints on the shadow size of Sgr A*.

prediction, we define the dimensionless parameter f_{SP} , which quantifies the deviation from the purely Schwarzschild precession ($f_{\text{SP}} = 1$),

$$f_{\text{SP}} = 1 + \frac{\Lambda c^4 a^4 (1 - e^2)^{3/2}}{6G^2 M^2} . \quad (10)$$

We compare this result with the measurements of the S2 orbit reported by the GRAVITY collaboration [39], which find $f_{\text{SP}} = 1.10 \pm 0.19$, as shown in Fig. 2. The current precision of the S2 precession measurement translates to an upper limit of $\Lambda \lesssim 10^{-36} \text{m}^{-2}$. We note that a more stringent constraint of $\Lambda \lesssim 10^{-46} \text{m}^{-2}$ was obtained by Benisty et al. [57] utilizing a joint post-Newtonian and dark energy framework.

3 Orbit Modelling

To model the stellar trajectories, we numerically integrate the full relativistic timelike geodesic equations in SdS spacetime, without relying on a post-Newtonian expansion. The radial motion is governed by the effective potential $V(r)$ appearing in Eq. (3). Bound motion exists when the particle is confined between two turning points, corresponding to the pericenter r_p and apocenter r_a , where $\dot{r} = 0$. The structure of the effective potential for different values of Λ is illustrated in Fig. 3. For sufficiently large Λ , the outer potential barrier is suppressed and bound orbits cease to exist.

The trajectory is obtained by integrating the geodesic equations,

$$\frac{d^2 x^\mu}{d\tau^2} + \Gamma_{\alpha\beta}^\mu \frac{dx^\alpha}{d\tau} \frac{dx^\beta}{d\tau} = 0 , \quad (11)$$

where the Christoffel symbols $\Gamma_{\alpha\beta}^\mu$ are computed from the SdS metric (2). We initialize the orbit at apocenter at the proper time $\tau = \tau_a$ in the equatorial plane ($\theta = \pi/2$). The initial phase-space vector is therefore,

$$\{x^\mu, \dot{x}^\mu\}_{\tau_a} = \{t_a, r_a, \pi/2, \varphi_a, \dot{t}_a, 0, 0, \dot{\varphi}_a\} . \quad (12)$$

The conserved E and L are uniquely determined by the semi-major axis a and eccentricity e . By evaluating the normalization condition (3) at the apsides $r_a = a(1 + e)$ and $r_p = a(1 - e)$,

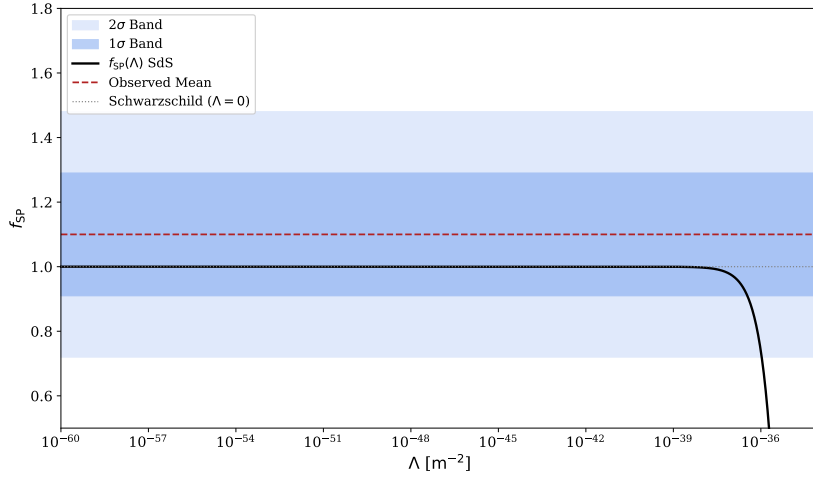


Figure 2: The plot for f_{SP} as a function of Λ . The shaded region denotes the constraint from GRAVITY observations [39]

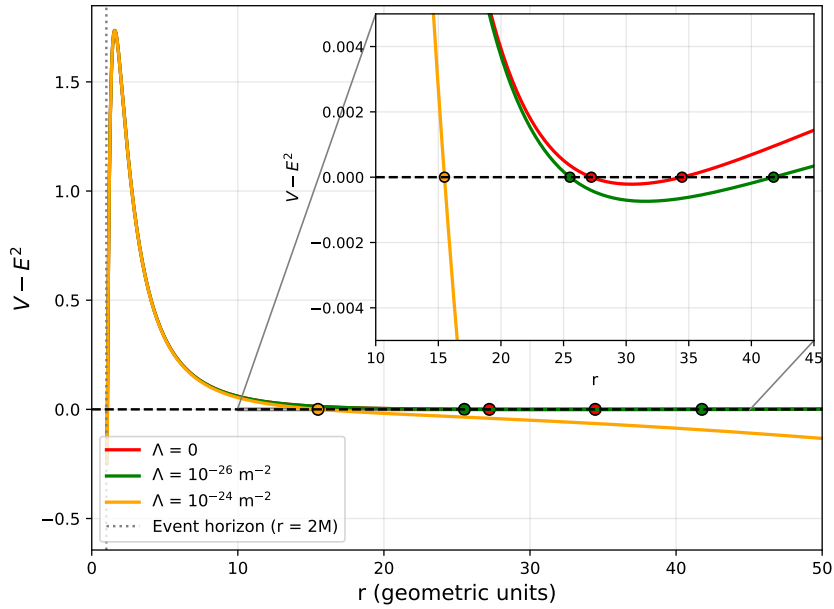


Figure 3: Effective potential $V(r)$ in SdS spacetime for different values of Λ . Bound motion occurs between the turning points r_p and r_a , which are highlighted with \bullet . For sufficiently large Λ (yellow curve), the outer potential barrier disappears, leading to unbound trajectories.

we find,

$$E = \sqrt{\frac{f(r_a)f(r_p)(r_a^2 - r_p^2)}{r_a^2 f(r_p) - r_p^2 f(r_a)}}, \quad L = \sqrt{\frac{r_a^2 r_p^2 (f(r_p) - f(r_a))}{r_a^2 f(r_p) - r_p^2 f(r_a)}}. \quad (13)$$

The initial velocities then follow from the conserved quantities through $\dot{t}_a = E/f(r_a)$ and $\dot{\varphi}_a = L/r_a^2$. The orbit is integrated both forward and backwards in proper time from τ_a using the adaptive high-order Runge-Kutta solver DOP853 [77].

3.1 Projection to Observer's Sky

The numerical integration of the geodesic equations yields the stellar trajectory $\{t(\tau), r(\tau), \varphi(\tau)\}$ along with the velocity components $u^\mu = \{u^t(\tau), u^r(\tau), u^\varphi(\tau)\}$. In the orbital plane ($z_{\text{orb}} = 0$), the Cartesian orbital position $\{x_{\text{orb}}, y_{\text{orb}}\}$ and velocity $\{v_{\text{orb}}^x, v_{\text{orb}}^y\}$ components are,

$$\begin{aligned} x_{\text{orb}} &= r \cos \varphi, & y_{\text{orb}} &= r \sin \varphi, \\ v_{\text{orb}}^x &= v_r \cos \varphi - v_\varphi \sin \varphi, & v_{\text{orb}}^y &= v_r \sin \varphi + v_\varphi \cos \varphi, \end{aligned} \quad (14)$$

where $v_r = u^r/u^t$ and $v_\varphi = ru^\varphi/u^t$ are the radial and azimuthal coordinate velocities, respectively. The transformation from the orbital plane to the observer sky frame is performed using the standard Thiele–Innes parametrization, specified by the inclination i , longitude of the ascending node Ω , and argument of periapsis ω . The corresponding Thiele–Innes elements (also called Innes constants) are [78],

$$\begin{aligned} A &= \cos \Omega \cos \omega - \sin \Omega \sin \omega \cos i, \\ B &= \sin \Omega \cos \omega + \cos \Omega \sin \omega \cos i, \\ C &= -\sin \omega \sin i, \\ F &= -\cos \Omega \sin \omega - \sin \Omega \cos \omega \cos i, \\ G &= -\sin \Omega \sin \omega + \cos \Omega \cos \omega \cos i, \\ H &= -\cos \omega \sin i. \end{aligned} \quad (15)$$

The projected sky coordinates and velocities are then obtained through

$$\begin{bmatrix} x^{\text{sky}} \\ y^{\text{sky}} \\ z^{\text{sky}} \end{bmatrix} = \mathcal{R} \begin{bmatrix} x_{\text{orb}} \\ y_{\text{orb}} \end{bmatrix}, \quad \begin{bmatrix} v_x^{\text{sky}} \\ v_y^{\text{sky}} \\ -v_z^{\text{sky}} \end{bmatrix} = \mathcal{R} \begin{bmatrix} v_{\text{orb}}^x \\ v_{\text{orb}}^y \end{bmatrix}, \quad (16)$$

where the matrix \mathcal{R} is given by,

$$\mathcal{R} = \begin{bmatrix} B & G \\ A & F \\ C & H \end{bmatrix}. \quad (17)$$

Here, $\{x^{\text{sky}}, y^{\text{sky}}\}$ denote the projected coordinates on the plane of the sky, while z^{sky} is the line-of-sight displacement relative to Sgr A*. We adopt the convention where z^{sky} points toward the observer, such that $v_z^{\text{sky}} > 0$ corresponds to approaching (blueshifted) motion. Finally, the observable angular coordinates, namely the Right Ascension (α) and Declination (δ), are obtained through the geometric projection,

$$\alpha = \tan^{-1} \left(\frac{x^{\text{sky}}}{D - z^{\text{sky}}} \right), \quad \delta = \tan^{-1} \left(\frac{y^{\text{sky}}}{D - z^{\text{sky}}} \right), \quad (18)$$

where D is the distance to Sgr A*. While the flat-sky approximation ($\alpha \simeq x^{\text{sky}}/D$) is typically sufficient, we retain the transcendental form.

3.2 Rømer delay

The varying line-of-sight position of the S-stars along their orbits induces a modulation in the light-travel time to the observer. This geometric effect gives rise to the Rømer delay, relating the emission time t_{em} to the observation time t_{obs} recorded at Earth through

$$t_{\text{em}} = t_{\text{obs}} - \frac{z^{\text{sky}}(t_{\text{em}})}{c}. \quad (19)$$

Since the stellar position z^{sky} depends on the orbital phase at emission, the equation must be solved iteratively at each observational epoch to determine the corresponding emission time [79].

We neglect the Shapiro delay in the present analysis. For the S-stars considered here, its contribution remains at most of order a few minutes, which is well below the temporal resolution of the available observations.

3.3 Reference Frame Motion

The infrared astrometric frame is tied to the radio reference frame of Sgr A* via SiO maser emission from nearby red giant stars, leading to small residual offsets and drifts relative to the black-hole rest frame [80]. To account for these effects, we include nuisance parameters corresponding to constant positional offsets (x_0, y_0) and linear proper-motion drifts (v_{x0}, v_{y0}) of the central mass. The theoretical sky coordinates evaluated at the observation time t_{obs} are therefore written as [38],

$$\begin{aligned} \alpha^{\text{th}}(t_{\text{obs}}) &= \alpha(t_{\text{em}}) + x_0 + v_{x0}(t_{\text{em}} - t_{\text{ref}}), \\ \delta^{\text{th}}(t_{\text{obs}}) &= \delta(t_{\text{em}}) + y_0 + v_{y0}(t_{\text{em}} - t_{\text{ref}}), \end{aligned} \quad (20)$$

where, t_{ref} denotes a reference epoch. In this work, it is chosen to coincide with the epoch of pericenter passage t_p for each star.

Similarly, the spectroscopic frame may contain a constant line-of-sight velocity offset. This is modelled through the nuisance parameter v_{z0} , which absorbs residual uncertainties associated in the Local Standard of Rest (LSR) correction and in the construction of the spectroscopic reference frame.

3.4 Relativistic Redshift

The observed spectroscopic redshift contains contributions from both the relativistic Doppler effect and gravitational time dilation. For a star moving in the SdS spacetime, the total redshift measured by a static distant observer is [81],

$$1 + \zeta_{\text{tot}} = \frac{1}{\sqrt{f(r_{\text{em}})}} \frac{\sqrt{1 - v^2/c^2}}{1 - v_z^{\text{sky}}/c}, \quad (21)$$

where $f(r_{\text{em}})$ is the metric function (2) evaluated at the emission radius, v is the total three-velocity magnitude, and v_z^{sky} is the line-of-sight velocity component in the sky-projected frame. The first factor represents the gravitational redshift in SdS spacetime, while the second incorporates the special-relativistic Doppler factor. The radial velocity is then given by, $v_R^{\text{th}} = c\zeta_{\text{tot}} + v_{z0}$, where v_{z0} denotes the constant spectroscopic velocity offset introduced the previous subsection.

To summarize, the numerical integration of the geodesic equations, together with the sky-plane projection, Rømer delay correction, reference-frame offsets, and relativistic redshift correction, provides the complete set of theoretical observables as a function of model parameters.

The model therefore predicts the astrometric coordinates in right ascension and declination $(\alpha, \delta) \equiv (\text{RA}^{\text{th}}, \text{Dec}^{\text{th}})$ and the radial velocity v_R^{th} . These quantities are subsequently assembled into the theoretical data vector used in the statistical analysis.

4 Data and Analysis

4.1 Data

We use astrometric and spectroscopic observations of S-stars orbiting Sgr A* spanning more than three decades. The 17-star dataset was published in [33], with all measurements available through the catalog [82]. Although S2 serves as our primary probe, we also include S1 and S14 to provide complementary constraints and consistency checks. The astrometric coordinates (RA, Dec) are reported in a reference frame centered approximately on the radio position of Sgr A*. At the reference epoch 2009.02, the origin of this frame has an uncertainty of approximately $\pm(0.2, 0.2)$ mas [80]. To account for residual calibration uncertainties between the astrometric frame and the dynamical center, we include nuisance parameters describing positional offsets and linear drifts in the orbital modelling introduced in the previous section.

4.1.1 S2 data

For S2, we use 145 astrometric measurements obtained between 1992.224 and 2016.53, together with 44 radial velocity measurements spanning 2000.487–2016.519 [33].

Pre-2002 data were acquired via the speckle-imaging camera SHARP at the ESO New Technology Telescope (NTT) [83], (precision ~ 3.8 mas). Post-2002 data utilize the adaptive-optics-assisted infrared camera NAOS+CONICA (NACO) [84, 85] at the Very Large Telescope (VLT) (precision $\sim 400 \mu\text{as}$).

Radial velocity measurements for S2 were obtained across two primary observational facilities. Pre-2003 data were collected using the NIRC2 adaptive-optics imager and spectrometer at the Keck Observatory [86]. From 2003 onward, measurements were acquired with the Spectrograph for INtegral Field Observations in the Near Infrared (SINFONI), an adaptive-optics-assisted integral field spectrograph at the VLT [87, 88].

4.1.2 S1, S14

To complement S2, we include two additional stars from the catalogue [82].

- **S1:** We utilize 161 astrometric positions (1992.224–2016.530) and 29 radial velocity measurements (2003.271–2016.519). While stars such as S54 and S24 have longer orbital periods but of the same order as S1 ($\gtrsim 166$ years), they were excluded from this analysis; S1 is uniquely retained as its data covers a larger fraction of its orbit.
- **S14:** With 99 astrometric positions (1992.224–2016.530) and 12 radial velocity measurements (2004.537–2016.284), S14 is notable for having one of the highest eccentricities in the sample ($e \sim 0.97$) [33].

4.2 Analysis

The relativistic orbit of S2 in SdS spacetime is modeled as a test particle orbiting the supermassive compact object Sgr A*. The system is characterized by a 14-dimensional parameter vector, Θ ,

$$\Theta = \{M, D, a, e, i, \Omega, \omega, t_p, x_0, y_0, v_{x0}, v_{y0}, v_{z0}, \Lambda\}, \quad (22)$$

where M and Λ are the spacetime parameters, D is the distance to the GC, and $\{a, e, i, \Omega, \omega, t_p\}$ are the orbital elements and $\{x_0, y_0, v_{x0}, v_{y0}, v_{z0}\}$ describe the astrometric and spectroscopic reference-frame offsets introduced in Section 3.

The observational data vector \mathcal{D} consists of the measured astrometric positions ($\text{RA}_j, \text{Dec}_j$) and radial velocities v_j^R at observation times t_j^{obs} . For a given parameter set Θ , the geodesic equations are integrated numerically using an adaptive solver, yielding a discrete sampling of the trajectory. In general, these integration points do not exactly coincide with the observational timestamps. We therefore construct a continuous representation of the orbit using cubic spline interpolation. Then, at each observation time t_j^{obs} , the corresponding emission time is obtained iteratively from the relation (19). The resulting theoretical vector $\mathcal{D}^{\text{th}}(\Theta)$ contains the predicted sky coordinates ($\text{RA}^{\text{th}}, \text{Dec}^{\text{th}}$) and radial velocities $v_{R,j}^{\text{th}}$ evaluated at the same observational epochs. Comparison between \mathcal{D} and $\mathcal{D}^{\text{th}}(\Theta)$ yields the astrometric and spectroscopic residuals used in likelihood analysis.

Parameter inference is performed within a Bayesian framework using Markov Chain Monte Carlo (MCMC) sampling. According to Bayes' Theorem, the posterior probability density $P(\Theta|\mathcal{D})$ is proportional to the product of the likelihood $\mathcal{L}(\mathcal{D}|\Theta)$ and the prior. Assuming independent Gaussian uncertainties, the total log-likelihood $\ln \mathcal{L}(\Theta)$ is written as the sum of independent astrometric and spectroscopic contributions,

$$\ln \mathcal{L}(\Theta) = -\frac{1}{2} [\chi_{\text{pos}}^2(\Theta) + \chi_{\text{vel}}^2(\Theta)] \quad , \quad (23)$$

where the χ^2 terms follow the standard definition:

$$\chi_{\text{pos,vel}}^2 = \sum_j \left(\frac{\mathcal{D}_j - \mathcal{D}_j^{\text{th}}(\Theta)}{\sigma_j} \right)^2 \quad . \quad (24)$$

Because the full relativistic geodesic equations are integrated directly, relativistic periapsis precession is automatically incorporated into the predicted trajectories. No additional precession term is therefore included in the likelihood. This treatment is consistent with the dataset used here [33], which predates the observational detection of Schwarzschild precession [39].

We perform independent parameter estimation for S2, S1, and S14 using the same 14-dimensional parameterization Θ . While the structure of Θ remains identical for all three stars, the prior distributions for the orbital elements are star-specific. For a positive Λ , we adopt a broad, uninformative prior on its logarithm,

$$\log_{10}(\Lambda/\text{m}^{-2}) \in [-70, -20] \quad . \quad (25)$$

This choice is sufficiently broad to allow the sampler to explore several orders of magnitude without imposing a preferred physical scale. For S2, we adopt uniform priors similar to those used in previous studies [40, 42, 47], as summarized in Table 2.

For S1 and S14, Gaussian priors on the black-hole mass M and GC distance D are adopted from the posterior constraints obtained in the S2 analysis (see Table 4). The logarithmic prior on Λ given in Eq. (25) is retained. We adopt a hybrid prior strategy for the remaining parameters. As summarized in Table 3, we assign Gaussian priors on the orbital elements centered on their literature values reported in [33]. The reference-frame offsets are assigned Gaussian priors motivated by [80], while the prior on the line-of-sight velocity offset v_{z0} is adopted from [33].

We initialize the MCMC walkers in the vicinity of the Maximum A Posteriori (MAP) estimate obtained through a preliminary optimization of the log-posterior using the L-BFGS-B algorithm [89]. The optimizer is initialized at the prior means while enforcing the parameter bounds defined by the adopted priors. Posterior sampling is subsequently performed using the affine-invariant ensemble sampler implemented in the `emcee` package [90].

Parameter	Uniform Prior
M ($10^6 M_\odot$)	[3, 5]
D (kpc)	[7, 9]
a (mas)	[110, 140]
e	[0.85, 0.9]
i ($^\circ$)	[130, 138]
Ω ($^\circ$)	[223, 231]
ω ($^\circ$)	[60, 70]
$t_p - 2002$ (yr)	[0.2, 0.4]
x_0 (mas)	[-10, 10]
y_0 (mas)	[-10, 10]
v_{x0} (mas yr $^{-1}$)	[-0.1, 0.1]
v_{y0} (mas yr $^{-1}$)	[-0.1, 0.1]
v_{z0} (km s $^{-1}$)	[-50, 50]

Table 2: Flat priors for S2 orbital parameter inference.

Parameter	S1		S14		Parameter	Mean	σ
	Mean	σ	Mean	σ			
M ($10^6 M_\odot$)					M ($10^6 M_\odot$)	4.17	0.19
D (kpc)					D (kpc)	8.00	0.19
a (mas)	595	24	286.3	3.6	x_0 (mas)	-0.2	0.01
e	0.5560	0.018	0.9761	0.0037	y_0 (mas)	0.1	0.2
i ($^\circ$)	119.14	0.21	100.59	0.87	v_{x0} (mas yr $^{-1}$)	0.05	0.1
ω ($^\circ$)	122.30	1.4	334.59	0.87	v_{y0} (mas yr $^{-1}$)	0.06	0.1
Ω ($^\circ$)	342.04	0.32	226.38	0.64	v_{z0} (km s $^{-1}$)	0.0	5.0
t_{peri} (yr)	2001.80	0.15	2000.12	0.06			

Table 3: Gaussian priors adopted for the Keplerian orbital elements of S1 and S14 from [33] (top). The black-hole mass and distance priors were taken from our S2 best-fit solution (Table 4), while the coordinate-system offsets and drift parameters were adopted from [80, 33] (bottom).

Parameter	This Work	[33]
M ($10^6 M_\odot$)	4.267 ± 0.201	4.10 ± 0.16
D (kpc)	8.141 ± 0.199	8.13 ± 0.15
a (mas)	128.68 ± 1.30	125.5 ± 0.9
e	0.88665 ± 0.00259	0.8839 ± 0.0019
i (deg)	133.78 ± 0.45	134.18 ± 0.40
ω (deg)	64.84 ± 0.66	65.51 ± 0.57
Ω (deg)	225.79 ± 0.67	226.94 ± 0.60
t_{peri} (yr)	2002.332 ± 0.006	2002.33 ± 0.01
x_0 (mas)	0.636 ± 0.301	-0.31 ± 0.34
y_0 (mas)	-2.189 ± 0.597	-1.29 ± 0.44
v_{x0} (mas yr $^{-1}$)	0.084 ± 0.036	0.078 ± 0.037
v_{y0} (mas yr $^{-1}$)	0.013 ± 0.045	0.126 ± 0.047
v_{z0} (km s $^{-1}$)	24.17 ± 7.12	8.9 ± 4.0
$\log_{10}(\Lambda/\text{m}^{-2})$	-52.93 ± 11.70	—

Table 4: Posterior mean values and 1σ uncertainties obtained from the MCMC analysis. The third column lists the corresponding values reported by [33].

Convergence of the chains is assessed using the integrated autocorrelation time [91], τ , for each parameter in Θ . The chains are considered converged when their total length satisfies $N > 100\tau$ and the estimated autocorrelation times remain stable during the final stages of sampling [90]. We additionally monitor the mean acceptance fraction of the walkers, which remains within the range 0.2–0.5 for all analyses, indicating efficient exploration of the parameter space. After convergence, the initial burn-in phase corresponding to more than five times the maximum autocorrelation time is discarded before constructing the final posterior distributions.

5 Results and Discussion

The posterior parameter constraints obtained from our MCMC analysis of the S2 star are summarized in Tables 4. The inferred mass of the central compact object $M = (4.27 \pm 0.2) \times 10^6 M_\odot$ and the distance to the GC $D = 8.14 \pm 0.2$ kpc are consistent within uncertainties with previous orbital analyses [33, 39]. The recovered orbital elements likewise agree well with earlier estimates, indicating that the SdS orbit model adequately describes the available astrometric and spectroscopic data. The resulting best-fit S2 orbit projected on the sky plane, along with the corresponding right ascension, declination, and radial velocity time series, are shown in Fig. 4. The marginalized posterior distributions of the fitted parameters with their respective confidence intervals are illustrated in Fig. 5.

Similarly, as emphasized in [33], meaningful constraints from S1 (and S14) require informative priors. Using Gaussian priors as described in Table 3, our analyses of S1 and S14 yield parameter estimates consistent with earlier determinations. In particular, the inferred M and D agree with those obtained from the S2 analysis within statistical uncertainties, despite the very different orbital configurations of these stars. A comparison of these results, together with the corresponding best-fit orbital trajectories for S1 and S14, is presented in Appendix C.

The inferred marginalized posterior distributions of $\log_{10}(\Lambda)$ are broad and distinctly non-Gaussian for all three stars. The posterior means happen to lie near the cosmological value inferred from large-scale observations [6]; however, this is not statistically meaningful and should not be interpreted as its local detection. The S-stars reside in a regime where attractive gravity dominates overwhelmingly and characteristic orbital periods satisfy $T_K \ll T_\Lambda$. Consequently, the likelihood becomes insensitive to sufficiently small values of Λ , rendering all values below a

Star	Median	$\log_{10}(\Lambda/\text{m}^{-2})_{68\%}$	$\Lambda_{68\%}$	$\log_{10}(\Lambda/\text{m}^{-2})_{95\%}$	$\Lambda_{95\%}$
S2	-53.18	< -46.85	$< 1.4 \times 10^{-47}$	< -37.28	$< 5.2 \times 10^{-38}$
S1	-53.56	< -47.60	$< 2.5 \times 10^{-48}$	< -38.59	$< 2.6 \times 10^{-39}$
S14	-52.92	< -46.89	$< 1.3 \times 10^{-47}$	< -37.74	$< 1.8 \times 10^{-38}$
Combined	-53.23	< -47.16	$< 6.9 \times 10^{-48}$	< -37.99	$< 1.0 \times 10^{-38}$

Table 5: Median values and upper credible limits on the cosmological constant obtained from the marginalized posterior distributions. The 68% and 95% bounds correspond to the cumulative posterior percentiles.

threshold sensitivity scale observationally indistinguishable within current precision.

The physically meaningful outcome of our analysis is therefore not a detection of a cosmological constant, but upper bounds on the magnitude of Λ . Since the marginalized posteriors are effectively one-sided toward small values of Λ , we derive upper credible limits directly from the cumulative posterior distributions *i.e.* from the integrated posterior probability. Combining the independent constraints obtained from S2, S1, and S14 yields an upper bound of $\Lambda \lesssim 6.9 \times 10^{-48} \text{m}^{-2}$ at 68% credibility and $\Lambda \lesssim 1.0 \times 10^{-38} \text{m}^{-2}$ at 95% credibility. The resulting median values and upper credible bounds for each star and for the combined constraint are summarized in Table 5.

The strongest constraint is obtained from S1, whose orbital period is approximately an order of magnitude larger than that of S2. This reflects the correspondence between orbital period and sensitivity to Λ , as pointed out in [57]. Although the S-stars orbit in a much stronger gravitational potential than Solar-System planets, their long orbital timescales imply sensitivity to comparable background curvature scales (from (1)). These bounds also show a significant improvement over the isolated precession estimate ($\sim 10^{-36} \text{m}^{-2}$) discussed in Section 2.2, demonstrating that fitting the full phase space of the trajectory provides substantially greater constraining power than using periapsis precession alone. The 68% credible upper limit is comparable to those reported in [57], where constraints of order 10^{-46}m^{-2} were obtained from periapsis-precession analyses of the Saturn and S2 orbits in the presence of both dark-energy and post-Newtonian corrections. Likewise, projected pulsar-timing studies for hypothetical S2-like pulsar orbiting Sgr A* reported sensitivity approaching $\Lambda \lesssim 9 \times 10^{-47} \text{m}^{-2}$ [92], owing to the extreme phase sensitivity of pulsar timing observables. The present analysis reaches a similar sensitivity scale using only stellar astrometry and spectroscopy. We further note that recent works have utilized neural networks frameworks to estimate limited parameters from the S2 orbit, reporting bounds of $\Lambda \lesssim 10^{-38} \text{m}^{-2}$ [93] and $\Lambda \leq 5.67 \times 10^{-40} \text{m}^{-2}$ [94]. These approaches rely on simplified or incomplete physical modelling of the underlying relativistic orbit. In contrast, our self-consistent orbital analysis, including full sky projections and relativistic corrections, yields substantially tighter bounds within the SdS framework.

6 Conclusions

In this work, we constrained the cosmological constant using the relativistic motion of the S2, S1, and S14 stars orbiting Sgr A*. The stellar trajectories were modelled through direct numerical integration of timelike geodesics in Schwarzschild-de Sitter spacetime, including relativistic redshift effects, Rømer delay corrections, and full sky-plane projection. Using publicly available astrometric and spectroscopic observations, we performed a Bayesian MCMC analysis to infer the orbital and spacetime parameters simultaneously.

The resulting posterior distributions show that current observations are insensitive to sufficiently small values of Λ , and therefore do not permit a local measurement of the cosmological constant. The physically relevant outcome of the analysis is instead the establishment of upper

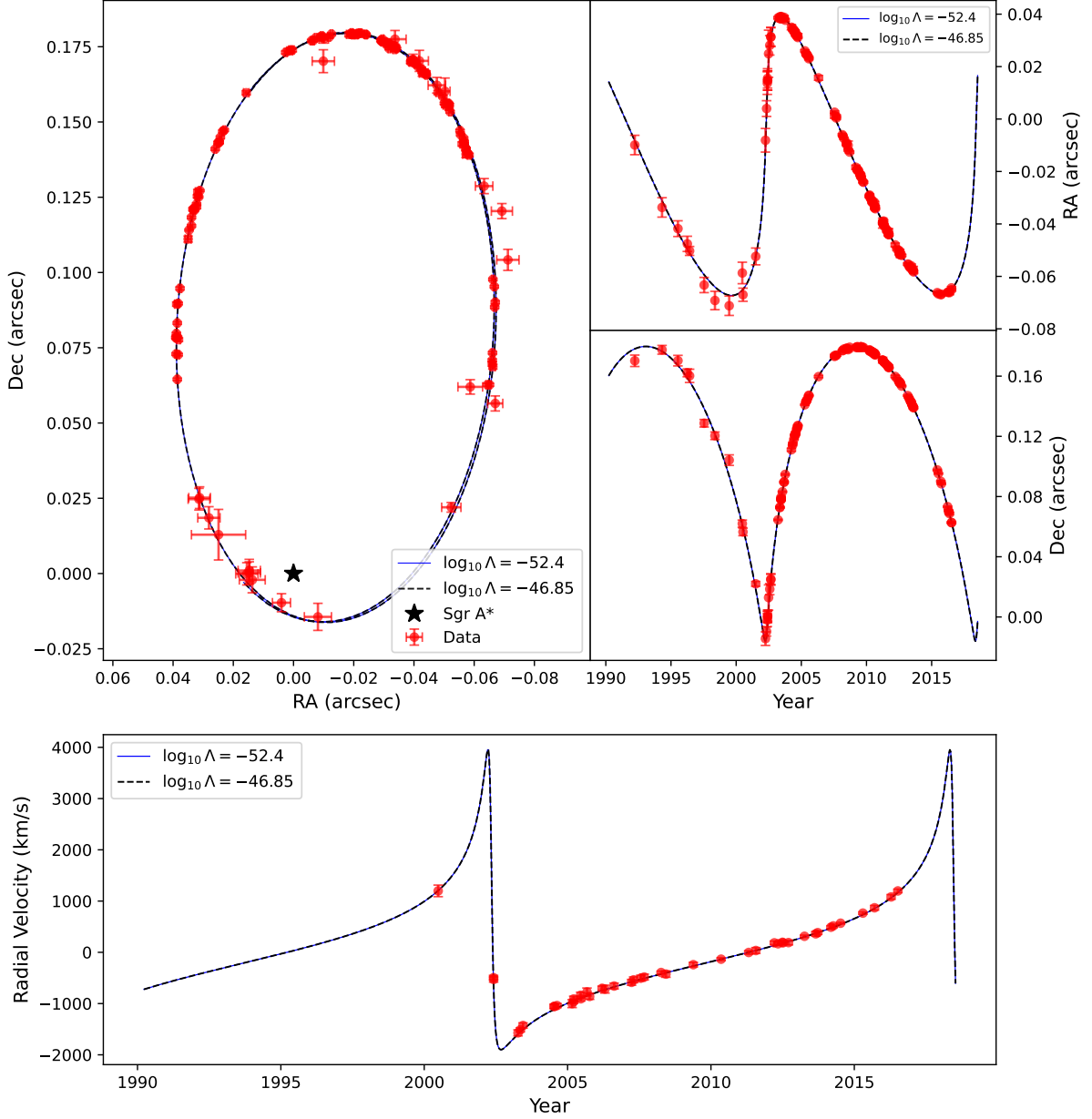


Figure 4: Astrometric and spectroscopic fits for the S2 orbit in SdS spacetime. The concatenated pre-2002 and post-2002 observational datasets are shown as red points with associated 1σ uncertainties (see Section 4.1.1). The solid curves correspond to the posterior mean model, while the dashed curves show the trajectory obtained using the 68% upper credible bound on Λ . The left panel displays the sky-projected orbit, while the right panels show the corresponding right ascension, declination, and radial-velocity evolution.

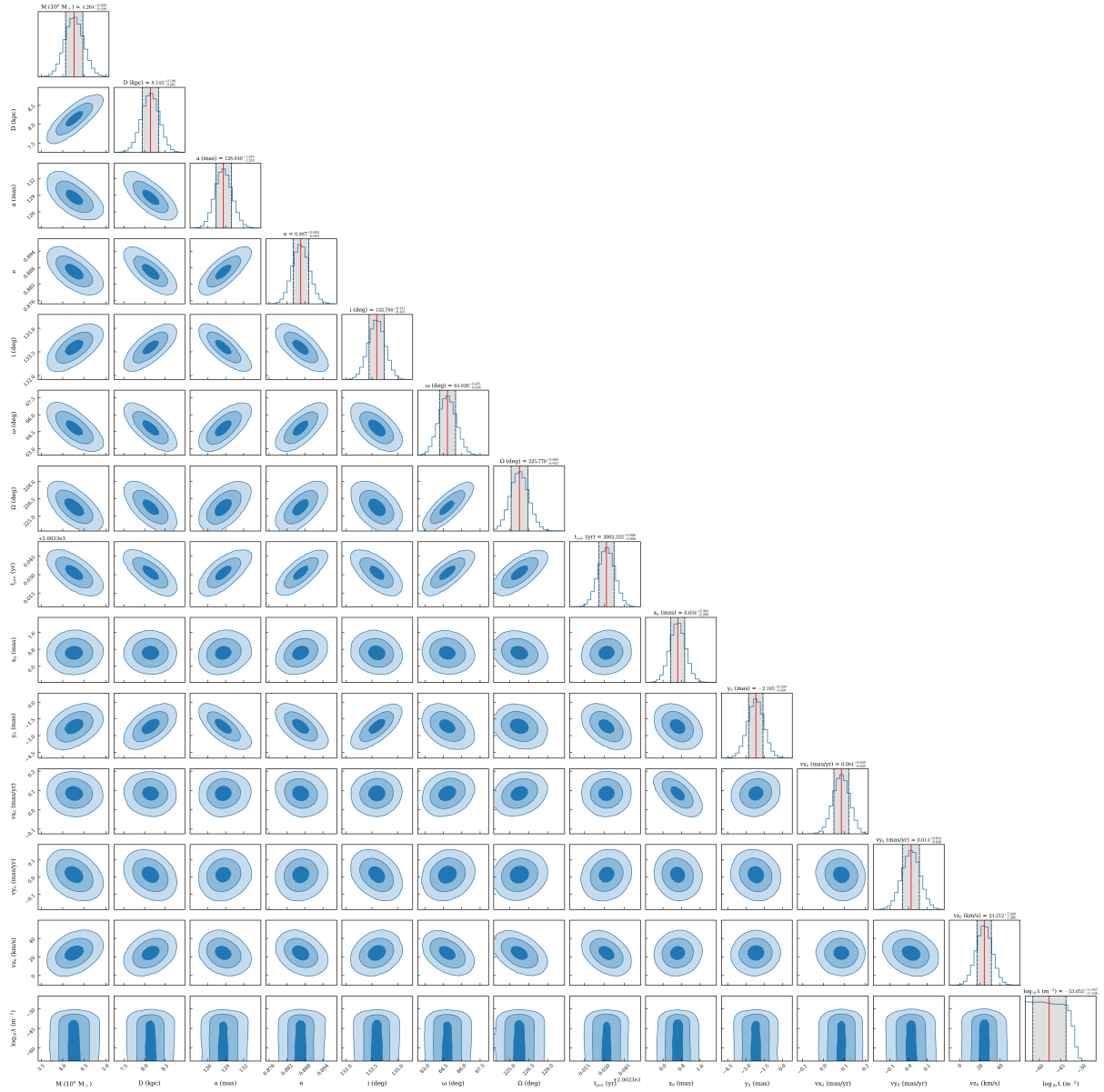


Figure 5: Marginalized posterior distribution contours with 68% (1σ), 95% (2σ), and 99.7% (3σ) confidence levels for the parameters modeling the S2 stellar orbit in SdS spacetime. The gray-shaded regions in the diagonal histograms correspond to the 1σ credible intervals around the parameter means. The posterior mean value and its symmetric 1σ range are printed above each column, with the corresponding interval boundaries indicated in the histograms by dashed vertical lines

bounds on Λ at the GC. The obtained constraints are significantly tighter than those derived from isolated periapsis-precession estimates, illustrating the advantage of fitting the complete relativistic orbital evolution.

Observations of S2 by the GRAVITY collaboration provide tight constraints on the mass distribution near Sgr A* [39, 95]. The in-plane, prograde Schwarzschild precession of S2 has been confirmed at $\sim 10\sigma$ confidence, limiting plausible extended-mass distributions (Plummer or power-law) within the orbit to $\sim 1200M_{\odot}$ (1σ) [95]. Stellar population models predict smaller masses even smaller masses in stars and in stellar remnants, with only a few to $\sim 10M_{\odot}$ near S2’s pericenter [35, 96, 97]. , comparable to the effective mass corresponding to our 95% upper limit on Λ . It is important to note that the extended mass produces retrograde precession while the Λ produces prograde precession, allowing the two effects to be distinguished.

Observations of S2 by the GRAVITY collaboration provide tight constraints on the mass distribution near Sgr A* [39]. The in-plane, prograde Schwarzschild precession of S2 has been confirmed at $\sim 10\sigma$ confidence, limiting plausible extended-mass distributions (Plummer or power-law) within the orbit to $\sim 1200 M_{\odot}$ (1σ) [95]. Furthermore, the stellar population models predict smaller masses in stars, in stellar remnants and only a few to $\sim 10 M_{\odot}$ near S2’s pericenter [96, 97, 35]. This realistic estimates are comparable to the effective mass corresponding to our 95% upper limit on Λ . However it is important to note that any extended mass distribution produces retrograde precession, Λ produces prograde precession.

Our analysis assumes a static and spherically symmetric spacetime and neglects both black-hole spin and perturbations from extended matter distributions near the Galactic Center. The consistent inclusion of these effects will be important for future high-precision studies. Longer-period S-stars and additional stellar populations in the central cluster may further enhance sensitivity to Λ by probing larger time scales. The GC occupies a unique regime different from Solar-System and cosmological scales, providing a complementary environment for placing local bounds on Λ through precision measurements of relativistic stellar orbits around Sgr A*.

Acknowledgements

The authors are grateful for discussions with Ranier Menote, David Benisty, Jenny Wagner, Ofek Birnholtz, Abdolali Banihashemi, and Davi Rodrigues. PHP acknowledges financial support from the Fundação de Amparo à Pesquisa e Inovação do Espírito Santo (FAPES, Brazil) and the Coordenação de Aperfeiçoamento de Pessoal de Nível Superior (CAPES, Brazil). WR acknowledges financial support from the CAPES. This work used the Sci-Com Lab of the Department of Physics at UFES, supported by FAPES, CAPES, and the Conselho Nacional de Desenvolvimento Científico e Tecnológico (CNPq, Brazil). DFM thanks the Research Council of Norway for their support and the resources provided by UNINETT Sigma2-the National Infrastructure for High-Performance Computing and Data Storage in Norway.

Data Availability

The data utilized in this study are publicly available from [33] and are electronically accessible through the catalogue [82].

References

- [1] Adam G. Riess et al. Observational evidence from supernovae for an accelerating universe and a cosmological constant. *Astron. J.*, 116:1009–1038, 1998.
- [2] S. Perlmutter et al. Measurements of Ω and Λ from 42 High Redshift Supernovae. *Astrophys. J.*, 517:565–586, 1999.

- [3] Shaun Cole et al. The 2dF Galaxy Redshift Survey: Power-spectrum analysis of the final dataset and cosmological implications. *Mon. Not. Roy. Astron. Soc.*, 362:505–534, 2005.
- [4] Daniel J. Eisenstein et al. Detection of the Baryon Acoustic Peak in the Large-Scale Correlation Function of SDSS Luminous Red Galaxies. *Astrophys. J.*, 633:560–574, 2005.
- [5] Shadab Alam et al. The clustering of galaxies in the completed SDSS-III Baryon Oscillation Spectroscopic Survey: cosmological analysis of the DR12 galaxy sample. *Mon. Not. Roy. Astron. Soc.*, 470(3):2617–2652, 2017.
- [6] N. Aghanim et al. Planck 2018 results. VI. Cosmological parameters. *Astron. Astrophys.*, 641:A6, 2020. [Erratum: *Astron. Astrophys.* 652, C4 (2021)].
- [7] R. Calderon et al. DESI 2024: reconstructing dark energy using crossing statistics with DESI DR1 BAO data. *JCAP*, 10:048, 2024.
- [8] A. G. Adame et al. DESI 2024 VII: cosmological constraints from the full-shape modeling of clustering measurements. *JCAP*, 07:028, 2025.
- [9] K. Lodha et al. Extended dark energy analysis using DESI DR2 BAO measurements. *Phys. Rev. D*, 112(8):083511, 2025.
- [10] M. Abdul Karim et al. DESI DR2 results. II. Measurements of baryon acoustic oscillations and cosmological constraints. *Phys. Rev. D*, 112(8):083515, 2025.
- [11] A. Chernin, P. Teerikorpi, and Yu. Baryshev. Why is the Hubble flow so quiet? *Advances in Space Research*, 31(2):459–467, January 2003.
- [12] Yuriy Baryshev, Arthur Chernin, and Pekka Teerikorpi. The Local Hubble flow: A Manifestation of dark energy. *Astron. Astrophys.*, 11 2000.
- [13] Igor D. Karachentsev, Arthur D. Chernin, and Pekka Teerikorpi. The Hubble Flow: Why does the cosmological expansion preserve its kinematical identity from a few Mpc distance to the observation horizon? *Astrofiz.*, 46:399, 2003.
- [14] Pekka Teerikorpi, Arthur D. Chernin, and Yuriy V. Baryshev. The Quiescent Hubble flow, local dark energy tests, and pairwise velocity dispersion in a $\Omega = 1$ Universe. *Astron. Astrophys.*, 440:791, 2005.
- [15] Arthur D. Chernin, Pekka Teerikorpi, Mauri J. Valtonen, G. Byrd, V. P. Dolgachev, and L. M. Domozhilova. Dark energy and the mass of the local group. *arXiv: Cosmology and Nongalactic Astrophysics*, 2009.
- [16] Arthur D. Chernin, Igor D. Karachentsev, Olga G. Nasonova, Pekka Teerikorpi, Mauri J. Valtonen, V. P. Dolgachev, L. M. Domozhilova, and G. Byrd. Dark energy domination in the virgocentric flow. *Astronomy and Astrophysics*, 520, 2010.
- [17] A. D. Chernin, N. V. Emelyanov, and I. D. Karachentsev. Dark energy domination in the local flow of giant galaxies. *Mon. Not. Roy. Astron. Soc.*, 449(2):2069–2078, 2015.
- [18] David Benisty, Anne-Christine Davis, and N. Wyn Evans. Constraining Dark Energy from the Local Group Dynamics. *Astrophys. J. Lett.*, 953(1):L2, 2023.
- [19] Alexander Silbergleit and Arthur Chernin. *Kepler Problem in the Presence of Dark Energy, and the Cosmic Local Flow*. SpringerBriefs in Physics. Springer, 2019.
- [20] F. D. Kahn and L. Woltjer. Intergalactic Matter and the Galaxy. *ApJ*, 130:705, November 1959.

- [21] James Binney and Scott Tremaine. *Galactic dynamics*. Princeton University Press, 1987.
- [22] Yang-Shyang Li and Simon D. M. White. Masses for the Local Group and the Milky Way. *Mon. Not. Roy. Astron. Soc.*, 384:1459–1468, 2008.
- [23] Candace Partridge, Ofer Lahav, and Yehuda Hoffman. Weighing the Local Group in the Presence of Dark Energy. *Mon. Not. Roy. Astron. Soc.*, 436:45, 2013.
- [24] Michael McLeod, Noam I. Libeskind, Ofer Lahav, and Yehuda Hoffman. Estimating the mass of the local group using machine learning applied to numerical simulations. *Journal of Cosmology and Astroparticle Physics*, 2017:034 – 034, 2016.
- [25] Pablo Lemos, Niall Jeffrey, Lorne Whiteway, Ofer Lahav, Noam I. Libeskind, and Yehuda Hoffman. Sum of the masses of the Milky Way and M31: A likelihood-free inference approach. *Phys. Rev. D*, 103(2):023009, 2021.
- [26] David Benisty. Weighing Milky Way and Andromeda in an expanding Λ CDM Universe - Decreasing the Local Group mass. *Astron. Astrophys.*, 689:L1, 2024.
- [27] David Benisty, Moshe M. Chaichian, and Anca Tureanu. Galaxy groups in the presence of cosmological constant: Increasing the masses of groups. *Phys. Lett. B*, 858:139033, 2024.
- [28] Kazunori Akiyama et al. First M87 Event Horizon Telescope Results. I. The Shadow of the Supermassive Black Hole. *Astrophys. J. Lett.*, 875:L1, 2019.
- [29] Kazunori Akiyama et al. First Sagittarius A* Event Horizon Telescope Results. I. The Shadow of the Supermassive Black Hole in the Center of the Milky Way. *Astrophys. J. Lett.*, 930(2):L12, 2022.
- [30] Sunny Vagnozzi et al. Horizon-scale tests of gravity theories and fundamental physics from the Event Horizon Telescope image of Sagittarius A. *Class. Quant. Grav.*, 40(16):165007, 2023.
- [31] A. M. Ghez, S. Salim, Seth D. Hornstein, A. Tanner, M. Morris, E. E. Becklin, and G. Duchene. Stellar orbits around the galactic center black hole. *Astrophys. J.*, 620:744–757, 2005.
- [32] A. Hees et al. Testing General Relativity with stellar orbits around the supermassive black hole in our Galactic center. *Phys. Rev. Lett.*, 118(21):211101, 2017.
- [33] S. Gillessen et al. An Update on Monitoring Stellar Orbits in the Galactic Center. *Astrophys. J.*, 837(1):30, 2017.
- [34] R. Abuter et al. Mass distribution in the Galactic Center based on interferometric astrometry of multiple stellar orbits. *Astron. Astrophys.*, 657:L12, 2022.
- [35] Reinhard Genzel, Frank Eisenhauer, and Stefan Gillessen. The galactic center massive black hole and nuclear star cluster. *Reviews of Modern Physics*, 82:3121–3195, 2010.
- [36] Reinhard Genzel. Nobel lecture: A forty-year journey. *Rev. Mod. Phys.*, 94:020501, 6 2022.
- [37] R. Abuter et al. Detection of the gravitational redshift in the orbit of the star S2 near the Galactic centre massive black hole. *Astron. Astrophys.*, 615:L15, 2018.
- [38] Tuan Do et al. Relativistic redshift of the star S0-2 orbiting the Galactic center supermassive black hole. *Science*, 365(6454):664–668, 2019.

- [39] R. Abuter et al. Detection of the Schwarzschild precession in the orbit of the star S2 near the Galactic centre massive black hole. *Astron. Astrophys.*, 636:L5, 2020.
- [40] Riccardo Della Monica, Ivan de Martino, and Mariafelicia de Laurentis. Orbital precession of the S2 star in Scalar–Tensor–Vector Gravity. *Mon. Not. Roy. Astron. Soc.*, 510(4):4757–4766, 2022.
- [41] Riccardo Della Monica, Ivan de Martino, and Mariafelicia de Laurentis. Constraining MODified Gravity with the S2 Star. *Universe*, 8(2):137, 2022.
- [42] Ivan de Martino, Riccardo della Monica, and Mariafelicia de Laurentis. f(R) gravity after the detection of the orbital precession of the S2 star around the Galactic Center massive black hole. *Phys. Rev. D*, 104(10):L101502, 2021.
- [43] Riccardo Della Monica, Ivan de Martino, Daniele Vernieri, and Mariafelicia de Laurentis. Testing horndeski gravity with S2 star orbit. *Mon. Not. Roy. Astron. Soc.*, 519(2):1981–1988, 2022.
- [44] Zelin Zhang, Songbai Chen, and Jiliang Jing. Constraining a disformal Schwarzschild black hole in DHOST theories with the orbit of the S2 star. *Eur. Phys. J. C*, 84(8):827, 2024.
- [45] Riccardo Della Monica and Ivan de Martino. Unveiling the nature of SgrA* with the geodesic motion of S-stars. *JCAP*, 03(03):007, 2022.
- [46] Parth Bambhaniya, Ashok B. Joshi, Dipanjan Dey, Pankaj S. Joshi, Arindam Mazumdar, Tomohiro Harada, and Ken-ichi Nakao. Relativistic orbits of S2 star in the presence of scalar field. *Eur. Phys. J. C*, 84(2):124, 2024.
- [47] César Navarrete, Fernando Vázquez-Chávez, Alejandro Cruz-Osorio, and Néstor Ortiz. Testing black hole space–times with the S2 star orbit: a Bayesian comparison. *Mon. Not. Roy. Astron. Soc.*, 546(3):stag059, 2026.
- [48] Parth Bambhaniya, Preet Dalal, Giovani H. Vicentin, Riccardo Della Monica, Elisabete M. de Gouveia Dal Pino, and Bina Patel. Testing the spacetime geometry of sgr a* with the relativistic orbit of s2 star, 2026.
- [49] Riccardo Della Monica and Ivan de Martino. Narrowing the allowed mass range of ultralight bosons with the S2 star. *Astron. Astrophys.*, 670:L4, 2023.
- [50] Riccardo Della Monica and Ivan de Martino. Bounding the mass of ultralight bosonic dark matter particles with the motion of the S2 star around Sgr A*. *Phys. Rev. D*, 108(10):L101303, 2023.
- [51] Zhao-Qiang Shen, Guan-Wen Yuan, Cheng-Zi Jiang, Yue-Lin Sming Tsai, Qiang Yuan, and Yi-Zhong Fan. Exploring dark matter spike distribution around the Galactic centre with stellar orbits. *Mon. Not. Roy. Astron. Soc.*, 527(2):3196–3207, 2023.
- [52] C. R. Argüelles, M. F. Mestre, E. A. Becerra-Vergara, V. Crespi, A. Krut, J. A. Rueda, and R. Ruffini. What does lie at the Milky Way centre? Insights from the S2-star orbit precession. *MNRAS*, 511(1):L35–L39, March 2022.
- [53] V. Crespi, C. R. Argüelles, E. A. Becerra-Vergara, M. F. Mestre, F. Peißker, J. A. Rueda, and R. Ruffini. The dynamics of S-stars and G-sources orbiting a supermassive compact object made of fermionic dark matter. *MNRAS*, 546(1):staf1854, February 2026.
- [54] Alexander F. Zakharov. Testing the Galactic Centre potential with S-stars. *MNRAS*, 513(1):L6–L9, 2022.

- [55] Valeria Kagramanova, Jutta Kunz, and Claus Lammerzahl. Solar system effects in Schwarzschild-de Sitter spacetime. *Phys. Lett. B*, 634:465–470, 2006.
- [56] Mauro Sereno and Philippe Jetzer. Solar and stellar system tests of the cosmological constant. *Phys. Rev. D*, 73:063004, 2006.
- [57] David Benisty, Jenny Wagner, and Denitsa Staicova. Dark energy as a critical period in binary motion: Bounds from multi-scale binaries. *Astron. Astrophys.*, 683:A83, 2024.
- [58] Philippe Jetzer and Mauro Sereno. Two-body problem with the cosmological constant and observational constraints. *Phys. Rev. D*, 73:044015, 2006.
- [59] Mustapha Ishak, Wolfgang Rindler, Jason Dossett, Jacob Moldenhauer, and Chris Allison. A New Independent Limit on the Cosmological Constant/Dark Energy from the Relativistic Bending of Light by Galaxies and Clusters of Galaxies. *Mon. Not. Roy. Astron. Soc.*, 388:1279–1283, 2008.
- [60] David Benisty, David Vasak, Jürgen Struckmeier, and Horst Stoecker. Bounding the cosmological constant using galactic rotation curves from SPARC dataset. *Phys. Rev. D*, 110(6):063028, 2024.
- [61] Adam G. Riess et al. A Comprehensive Measurement of the Local Value of the Hubble Constant with $1 \text{ km s}^{-1} \text{ Mpc}^{-1}$ Uncertainty from the Hubble Space Telescope and the SH0ES Team. *Astrophys. J. Lett.*, 934(1):L7, 2022.
- [62] Dillon Brout et al. The Pantheon+ Analysis: Cosmological Constraints. *Astrophys. J.*, 938(2):110, 2022.
- [63] Friedrich Kottler. Über die physikalischen Grundlagen der Einsteinschen Gravitationstheorie. *Annalen Phys.*, 361(14):401–462, 1918.
- [64] Z. Stuchlík and S. Hledík. Some properties of the Schwarzschild-de Sitter and Schwarzschild-anti-de Sitter spacetimes. *Phys. Rev. D*, 60(4):044006, August 1999.
- [65] Alexander F. Zakharov. Are signatures of anti-de-sitter black hole at the galactic center?, 2014.
- [66] Reginaldo Prado-Fuentes, Rodrigo Aros, Milko Estrada, and Bastian Astudillo. Constructing Regular Lovelock Black Holes with Degenerate Vacuum and $\Lambda < 0$ Using the Gravitational Tension—Shadow Analysis. *Universe*, 11(10):338, 2025.
- [67] Wolfgang Rindler. *Relativity: special, general, and cosmological*. Oxford University Press, 2001.
- [68] Volker Perlick and Oleg Yu. Tsupko. Calculating black hole shadows: Review of analytical studies. *Phys. Rept.*, 947:1–39, 2022.
- [69] Javad T. Firouzjaee and Alireza Allahyari. Black hole shadow with a cosmological constant for cosmological observers. *Eur. Phys. J. C*, 79(11):930, 2019.
- [70] Rittick Roy and Sayan Chakrabarti. Study on black hole shadows in asymptotically de Sitter spacetimes. *Phys. Rev. D*, 102(2):024059, 2020.
- [71] Volker Perlick, Oleg Yu. Tsupko, and Gennady S. Bisnovaty-Kogan. Black hole shadow in an expanding universe with a cosmological constant. *Phys. Rev. D*, 97(10):104062, 2018.
- [72] G. S. Bisnovaty-Kogan, O. Yu. Tsupko, and V. Perlick. Shadow of a black hole at local and cosmological distances. *PoS*, MULTIF2019:009, 2019.

- [73] Andrew W. Kerr, John C. Hauck, and Bahram Mashhoon. Standard clocks, orbital precession and the cosmological constant. *Class. Quant. Grav.*, 20:2727, 2003.
- [74] Lorenzo Iorio. Solar System motions and the cosmological constant: A New approach. *Adv. Astron.*, 2012:268647, 2012. [Erratum: *Adv.Astron.* 2012, 507892 (2012)].
- [75] Matteo Luca Ruggiero. Perturbations of Keplerian Orbits in Stationary Spherically Symmetric Spacetimes. *Int. J. Mod. Phys. D*, 23:1450049, 2014.
- [76] Hideyoshi Arakida. Note on the perihelion/periastron advance due to cosmological constant. *Int. J. Theor. Phys.*, 52:1408–1414, 2013.
- [77] Ernst Hairer, Syvert Paul Nørsett, and Gerhard Wanner. *Solving Ordinary Differential Equations I: Nonstiff Problems*, volume 8 of *Springer Series in Computational Mathematics*. Springer-Verlag, Berlin, Heidelberg, 2 edition, 1993.
- [78] W. D. Heintz. *Double stars*, volume 15 of *GEOPHYSICS AND ASTROPHYSICS MONOGRAPHS, AN INTERNATIONAL SERIES OF FUNDAMENTAL TEXTBOOKS*. D. Reidel Publishing Company, DORDRECHT, HOLLAND / BOSTON, U.S.A/ LONDON, ENGLAND, 1978.
- [79] Sanjar Shaymatov, Bobomurat Ahmedov, Mariafelicia De Laurentis, Mubasher Jamil, Qiang Wu, Anzhong Wang, and Mustapha Azreg-Aïnou. On the Parameters of the Spherically Symmetric Parameterized Rezzolla–Zhidenko Spacetime through Solar System Tests, the Orbit of the S2 Star about Sgr A*, and Quasiperiodic Oscillations. *Astrophys. J.*, 959(1):6, 2023.
- [80] P. M. Plewa, S. Gillessen, F. Eisenhauer, T. Ott, O. Pfuhl, E. George, J. Dexter, M. Habibi, R. Genzel, M. J. Reid, and K. M. Menten. Pinpointing the near-infrared location of Sgr A* by correcting optical distortion in the NACO imager. *MNRAS*, 453(3):3234–3244, November 2015.
- [81] M. Grould, F. H. Vincent, T. Paumard, and G. Perrin. General relativistic effects on the orbit of the S2 star with GRAVITY. *Astron. Astrophys.*, 608:A60, 2017.
- [82] Stefan Gillessen, Philipp M. Plewa, Frank Eisenhauer, R. Sari, Idel Waisberg, Maryam Habibi, Oliver Pfuhl, E. M. George, Jason Dexter, S. D. von Fellenberg, Thomas Ott, and Reinhard Genzel. 25yrs monitoring of stellar orbits in the gc. *Centre de Données astronomique de Strasbourg (CDS)*, 2016.
- [83] R. Hofmann, A. Eckart, R. Genzel, and S. Drapatz. High Resolution K-Band Images of the Galactic Centre. *Astrophysics and Space Science*, 205(1):1–4, July 1993.
- [84] Rainer Lenzen, Reiner Hofmann, Peter Bizenberger, and Andreas Tusche. CONICA: the high-resolution near-infrared camera for the ESO VLT. In Albert M. Fowler, editor, *Infrared Astronomical Instrumentation*, volume 3354 of *Society of Photo-Optical Instrumentation Engineers (SPIE) Conference Series*, pages 606–614, August 1998.
- [85] Gerard Rousset, Francois Lacombe, Pascal Puget, Norbert N. Hubin, Eric Gendron, Jean-Marc Conan, Pierre Y. Kern, Pierre-Yves Madec, Didier Rabaud, David Mouillet, Anne-Marie Lagrange, and Francois J. Rigaut. Design of the Nasmyth adaptive optics system (NAOS) of the VLT. In Domenico Bonaccini and Robert K. Tyson, editors, *Adaptive Optical System Technologies*, volume 3353 of *Society of Photo-Optical Instrumentation Engineers (SPIE) Conference Series*, pages 508–516, September 1998.

- [86] F. Eisenhauer, R. Schoedel, R. Genzel, T. Ott, M. Tecza, R. Abuter, A. Eckart, and T. Alexander. A geometric determination of the distance to the galactic center. *Astrophys. J. Lett.*, 597:L121–L124, 2003.
- [87] Frank Eisenhauer et al. Sinfoni - integral field spectroscopy at 50 milli-arcsecond resolution with the eso vlt. *Proc. SPIE Int. Soc. Opt. Eng.*, 4841:1548–1561, 2003.
- [88] Henri Bonnet, Robert Abuter, Andrew Baker, Walter Bornemann, Anthony Brown, Roberto Castillo, Ralf Conzelmann, Romuald Damster, Richard Davies, Bernard Delabre, Rob Donaldson, Christophe Dumas, Frank Eisenhauer, Eddie Elswijk, Enrico Fedrigo, Gert Finger, Hans Gemperlein, Reinhard Genzel, Andrea Gilbert, Gordon Gillet, Armin Goldbrunner, Matthew Horrobin, Rik Ter Horst, Stefan Huber, Norbert Hubin, Christof Iserlohe, Andreas Kaufer, Markus Kissler-Patig, Jan Kragt, Gabby Kroes, Matthew Lehnert, Werner Lieb, Jochen Liske, Jean-Louis Lizon, Dieter Lutz, Andrea Modigliani, Guy Monnet, Nicole Nesvadba, Jona Patig, Johan Pragt, Juha Reunanen, Claudia Röhrle, Silvio Rossi, Riccardo Schmutzer, Ton Schoenmaker, Jürgen Schreiber, Stefan Stroebele, Thomas Szeifert, Linda Tacconi, Matthias Tecza, Niranjan Thatte, Sebastien Tordo, Paul van der Werf, and Harald Weisz. First light of SINFONI at the VLT. *The Messenger*, 117:17–24, September 2004.
- [89] Byrd Richard H., Lu Peihuang, Necedal Jorge, and Zhu Ciyou. A Limited Memory Algorithm for Bound Constrained Optimization. *SIAM J. Sci. Comput.*, 16(5):1190–1208, 2006.
- [90] Daniel Foreman-Mackey, David W. Hogg, Dustin Lang, and Jonathan B. Goodman. emcee: The mcmc hammer. *Publications of the Astronomical Society of the Pacific*, 125:306 – 312, 2012.
- [91] Jonathan Goodman and Jonathan Weare. Ensemble samplers with affine invariance. *Communications in Applied Mathematics and Computational Science*, 5(1):65–80, January 2010.
- [92] Lorenzo Iorio. Perspectives on constraining a cosmological constant-type parameter with pulsar timing in the Galactic Center. *Universe*, 4(4):59, 2018.
- [93] N. Galikyan, Sh. Khlghatyan, Armen Kocharyan, and V. G. Gurzadyan. Neural network analysis of s-star dynamics: implications for modified gravity. *The European Physical Journal Plus*, 138, 2023.
- [94] Shinsei Eyama and Youhei Masada. Constraining the cosmological constant from stellar orbits around sgr a* using physics-informed neural networks, 2025.
- [95] Karim Abd El Dayem et al. Improving constraints on the extended mass distribution in the Galactic center with stellar orbits. *Astron. Astrophys.*, 692:A242, 2024.
- [96] Tal Alexander. Stellar dynamics and stellar phenomena near a massive black hole. *Annual Review of Astronomy and Astrophysics*, 55(1):17–57, August 2017.
- [97] H. Baumgardt, P. Amaro-Seoane, and R. Schödel. The distribution of stars around the milky way’s central black hole: Iii. comparison with simulations. *Astronomy & Astrophysics*, 609:A28, December 2017.

A Angular shadow size in SdS

The SdS metric possesses a black hole horizon r_h and a cosmological horizon r_c (with $r_h < r_c$), where $f(r_h) = f(r_c) = 0$. Static observers are restricted to the region $r_h < r < r_c$ where $f(r) >$

0. Unlike asymptotically flat Schwarzschild spacetime, SdS admits no accessible asymptotic region for static observers; instead, the cosmological horizon acts as the outer causal boundary. Consequently, the large-distance behaviour of the shadow is determined relative to this finite boundary rather than an observer at null infinity.

The angular radius of the shadow for a static observer at radius r_O follows from the local optical geometry of null rays [68] (also see [72] for visualizations),

$$\sin^2 \vartheta = \frac{(L/E)^2 g_{tt}(r_O)}{g_{\varphi\varphi}(r_O)} = \frac{b^2 f(r_O)}{r_O^2}. \quad (26)$$

Setting $b = b_{\text{crit}}$ from (6) into this angular relation yields the shadow angle,

$$\sin^2 \vartheta_{\text{sh}} = \frac{27(GM/c^2)^2}{r_O^2} \frac{f(r_O)}{1 - 9\Lambda(GM/c^2)^2}. \quad (27)$$

For $\Lambda = 0$, this reduces to the Schwarzschild result, where the shadow angle vanishes as $r_O \rightarrow \infty$. In SdS, however, the large-distance limit is replaced by the cosmological horizon. In the limit $r_O \rightarrow r_c$, one has $f(r_O) \rightarrow 0$, and hence $\sin^2 \vartheta_{\text{sh}} \rightarrow 0$. Thus, the shadow disappears at the cosmological horizon.

For realistic observers at large but still sub-horizon distances ($r_O \ll r_c$), we can expand $f(r_O)$,

$$\sin^2 \vartheta_{\text{sh}} \approx \frac{27(GM/c^2)^2}{r_O^2(1 - 9\Lambda(GM/c^2)^2)} \left(1 - \frac{\Lambda r_O^2}{3} + \dots\right). \quad (28)$$

The Λ -correction decreases the shadow size relative to the Schwarzschild case at the same coordinate radius. In the small-angle limit, the shadow radius $r_{\text{sh}} = \vartheta_{\text{sh}} r_O$ reduces to $r_{\text{sh}} \approx b_{\text{crit}} \sqrt{f(r_O)}$ reproducing equation (8).

The discussion above applies to static observers located at a fixed radial coordinate r_O . In a cosmological setting, however, a more natural choice is a comoving observer. For comoving observers, the angular size of the shadow does not vanish at large distances like in the static case; instead, it approaches a finite limiting value [71, 72].

B Periapsis Precession in SdS

We provide a simple, first-order perturbative derivation of the influence of the cosmological constant Λ on the periapsis advance of a timelike orbit to supplement (9). Similar derivations leading to this result have appeared in several works [73, 74, 75, 76, 57]. Starting from the exact second-order geodesic equation for a timelike particle ($\epsilon = 1$), (4),

$$\frac{d^2 u}{d\varphi^2} + u = \frac{GM}{L^2} + \frac{3GM}{c^2} u^2 - \frac{\Lambda c^2}{3L^2 u^3}, \quad (29)$$

we treat both the Schwarzschild correction ($3GMu^2/c^2$) and the Λ term as first-order perturbations to the classical Kepler problem. Neglecting these relativistic corrections yields the Newtonian solution $u_N(\varphi) = \frac{1}{p}(1 + e \cos \varphi)$ where, $p \equiv \frac{L^2}{GM} = a(1 - e^2)$ is the semi-latus rectum of the orbit.

The perturbative framework is valid under conditions $\frac{GM}{c^2 p} \ll 1$ and $\Lambda p^2 \ll 1$. We write the full solution as $u = u_N + u_1$ where u_1 represents a small first-order correction. Since the relativistic source terms are already first order, it is sufficient to evaluate them using the unperturbed profile $u_N(\varphi)$. So in the non-linear source terms, u_1 terms may consistently be neglected and to first order we can replace $u^2 \rightarrow u_0^2$ and $u^{-3} \rightarrow u_0^{-3}$.

A slowly precessing orbit is given by $u(\varphi) = \frac{1}{p} [1 + e \cos((1 - \delta)\varphi)]$ where $\delta \ll 1$ is the fractional shift in orbital frequency. The corresponding periapsis advance per orbit is therefore $\Delta\varphi = 2\pi\delta$. Substituting this ansatz into the left-hand side of the geodesic equation and expanding to first order in δ gives,

$$\frac{d^2u}{d\varphi^2} + u = \frac{1}{p} + \frac{2e\delta}{p} \cos((1 - \delta)\varphi) \approx \frac{GM}{L^2} + \frac{2e\delta}{p} \cos \varphi . \quad (30)$$

Expressing the source terms up to linear order,

$$\begin{aligned} \frac{3GM}{c^2}u_0^2 &\simeq \frac{3GM}{c^2p^2} + \frac{6GMe}{c^2p^2} \cos \varphi, \\ -\frac{\Lambda c^2}{3L^2u_0^3} &\simeq -\frac{\Lambda c^2p^3}{3L^2} + \frac{\Lambda c^2p^3}{L^2}e \cos \varphi , \end{aligned} \quad (31)$$

and collecting the resonant $\cos \varphi$ terms on both sides of the equation, we establish,

$$\delta = \frac{3GM}{c^2p} + \frac{\Lambda c^2p^3}{2GM} . \quad (32)$$

The total periapsis advance per complete orbital period is therefore given by:

$$\Delta\varphi = 2\pi\delta = \frac{6\pi GM}{c^2p} + \frac{\pi\Lambda c^2p^3}{GM} , \quad (33)$$

which matches (9).

C Results for S1 and S14

Here we present the full posterior constraints obtained from the independent analyses of the S1 and S14 trajectories and in particular the consistency of the independently inferred values of M and D . The stars S1 and S14 probe very different orbital regimes. S14 follows a highly eccentric and tightly bound orbit, whereas S1 traces a longer-period orbit. Despite these differences in orbital geometry and dynamical timescales, all three systems converge toward compatible estimates of the global parameters M and D .

The complete posterior parameter estimates for S1 and S14 are listed in Table 6. The corresponding best-fit orbital trajectories and radial-velocity fits are shown in Figs. 6 and 7. The inferred values of the parameters are consistent, within uncertainties, with the estimates of [33]. In particular, the global parameters M , D from S1 and S14 agree with those derived from S2 analysis. The corresponding posterior distributions are shown in Fig. 8, while Fig. 9 compares our inferred values with the orbital analyses of [33] and [39]. The reduced chi-squared values are $\chi_\nu^2 = 0.91$ for S2, $\chi_\nu^2 = 0.75$ for S1 and $\chi_\nu^2 = 1.03$ for S14, indicating that the relativistic SdS framework provides an adequate description of the astrometric and spectroscopic observations within the reported uncertainties. The slightly lower value for S1 may reflect a stronger prior dependence of that fit.

Parameter	S1	S14
M ($10^6 M_\odot$)	4.060 ± 0.120	4.222 ± 0.170
D (kpc)	8.135 ± 0.081	8.100 ± 0.119
a (mas)	609.63 ± 11.01	298.17 ± 2.57
e	0.57054 ± 0.00781	0.96887 ± 0.00151
i (deg)	119.685 ± 0.137	99.985 ± 0.403
ω (deg)	121.808 ± 0.596	335.247 ± 0.690
Ω (deg)	342.409 ± 0.197	226.831 ± 0.319
t_{peri} (yr)	2001.648 ± 0.072	2000.037 ± 0.030
x_0 (mas)	-0.200 ± 0.010	-0.200 ± 0.010
y_0 (mas)	0.089 ± 0.199	0.107 ± 0.196
v_{x0} (mas yr $^{-1}$)	0.024 ± 0.076	0.116 ± 0.084
v_{y0} (mas yr $^{-1}$)	0.103 ± 0.094	0.084 ± 0.086
v_{z0} (km s $^{-1}$)	1.49 ± 4.92	1.10 ± 4.98
$\log_{10}(\Lambda/\text{m}^{-2})$	-53.50 ± 11.23	-53.01 ± 11.55

Table 6: Posterior mean values and corresponding 1σ uncertainties for S1 and S14

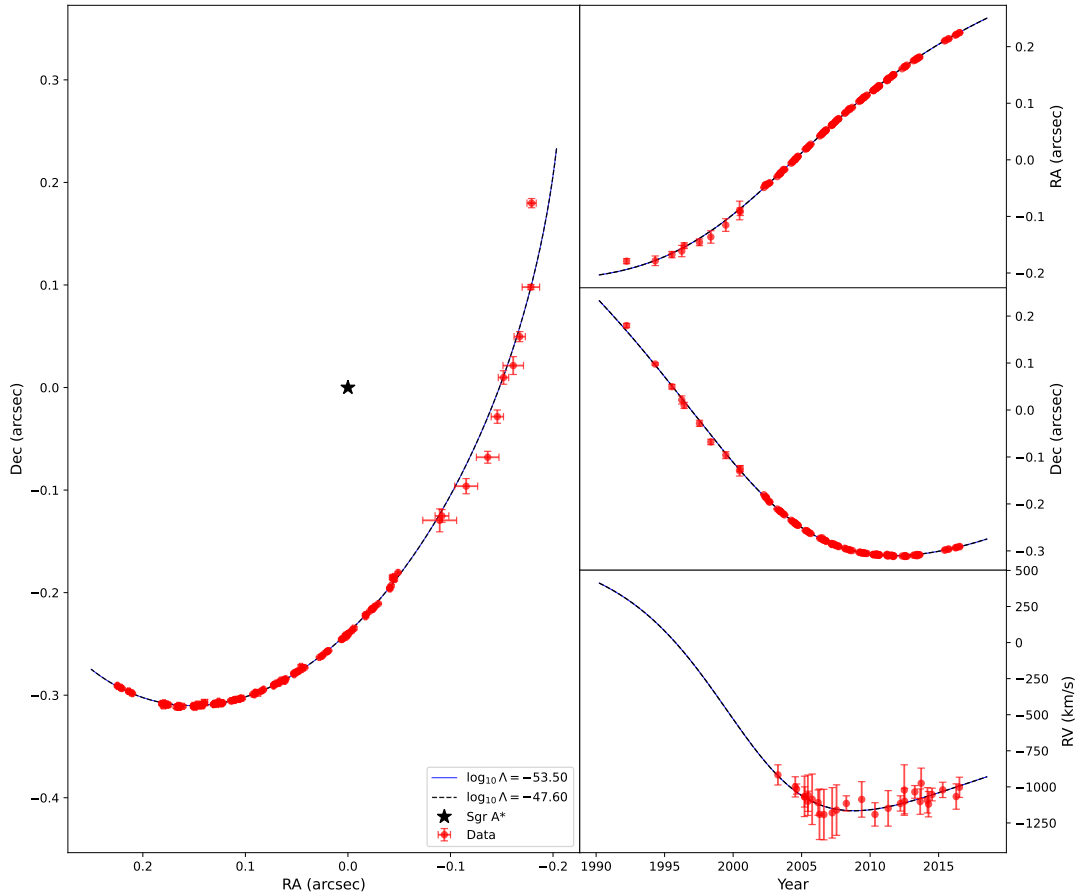


Figure 6: Best-fit SdS orbit for S1. The figure shows the projected sky trajectory together (left) with the corresponding right ascension, declination, and radial-velocity fits (right) to the observational data. As in Fig. 4, both the posterior mean trajectory and the orbit corresponding to the 68% upper credible bound on Λ are shown.

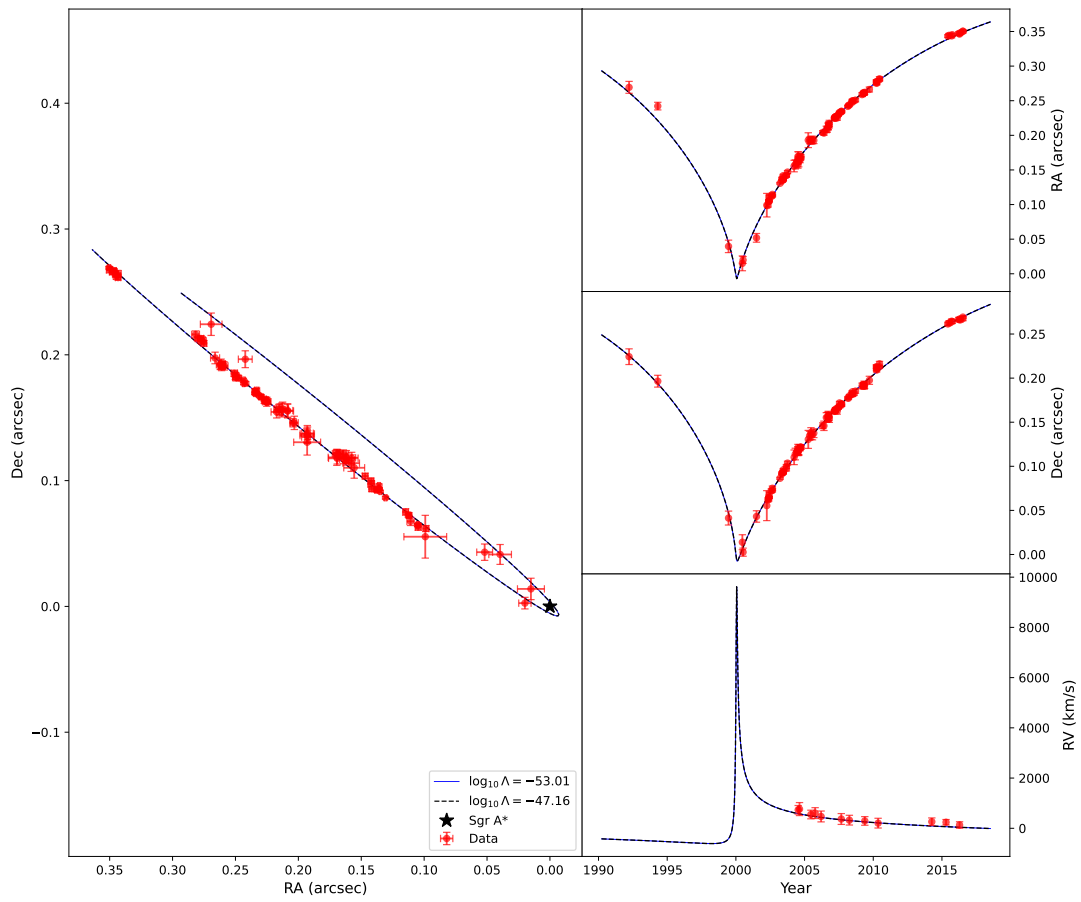


Figure 7: Same as Fig. 6, but for the S14 star.

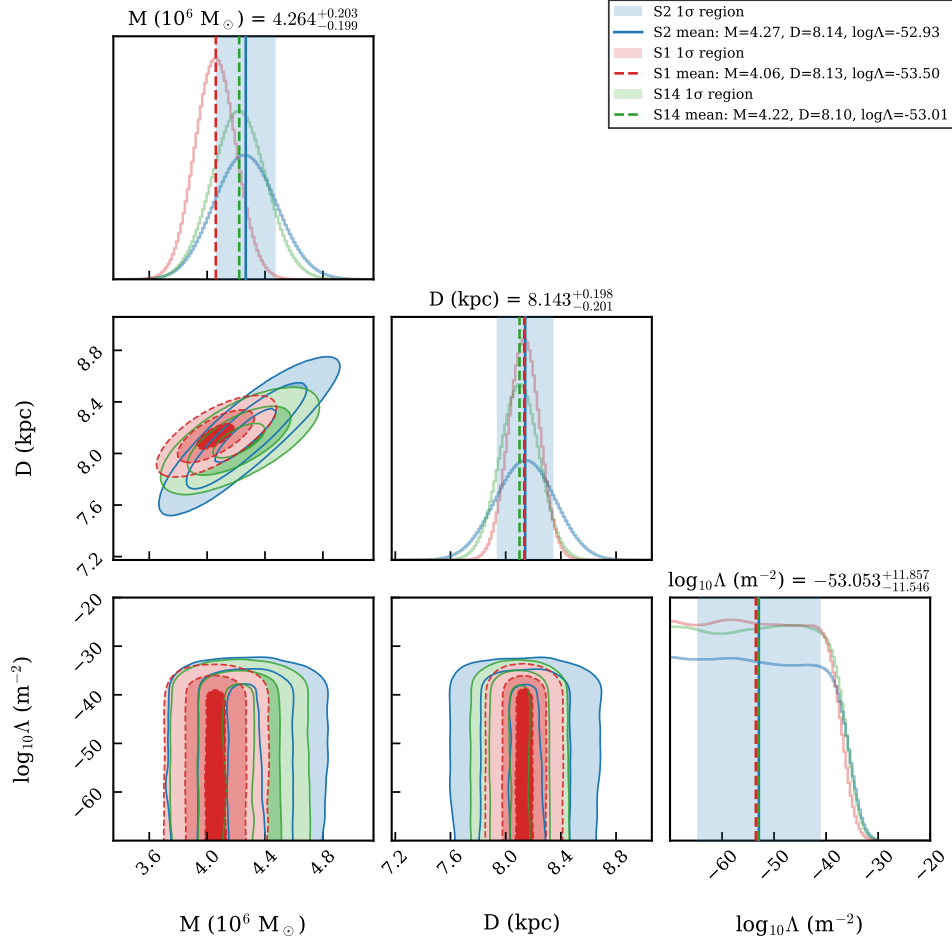


Figure 8: Marginalized posterior distributions for M, D and Λ obtained from the S2, S1, and S14 orbital analyses (in blue, red and green respectively). The contours indicate the $1\sigma, 2\sigma$ and 3σ confidence levels for the parameters.

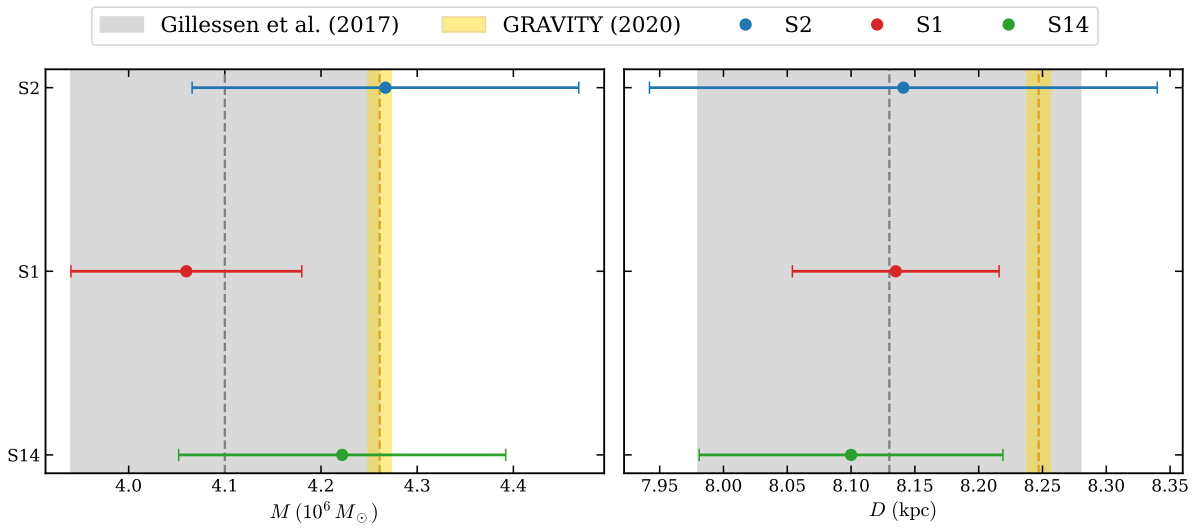


Figure 9: Comparison of the inferred black-hole mass M and Galactic Center distance D obtained in this work from S2, S1, and S14 with previous measurements from [33] and [39]. Error bars correspond to 1σ uncertainties.